Confidence Weighted Local Phase Features for Robust Bone Surface Segmentation in Ultrasound

Niamul Quader[1], Antony Hodgson[2], and Rafeef Abugharbieh[1]

[1] Department of Electrical and Computer Engineering
[2] Department of Mechanical Engineering, The University of British Columbia, Vancouver, BC, Canada
niamul@ece.ubc.ca, ahodgson@mech.ubc.ca, rafeef@ece.ubc.ca

Abstract. Ultrasound (US) image guidance in orthopaedic surgery is emerging as a viable non-invasive alternative to the currently dominant radiation-based modalities. Though it offers many advantages including reduced imaging costs and safer operation, the relatively low US image quality complicates data processing and visualization. We propose a novel approach for robust bone localization that integrates multiple US image features including local phase information, local signal attenuation, and bone shadowing to robustly segment bone surfaces. We demonstrate the advantages of our approach in different contexts including improved segmentation quality, increased registration accuracy, and decreased sensitivity to parameter setting. We present quantitative and qualitative validation on a bovine femur phantom and on real-life clinical pelvis US data from 18 trauma patients using computed tomography (CT) image sets as ground truth.

Keywords: ultrasound, local phase features, shadowing effect, confidence map, orthopaedic imaging, segmentation, bone imaging.

1 Introduction

Ultrasound (US) bone imaging is receiving increasing attention in computer assisted orthopaedic surgery (CAOS) applications. The primary motivation is reducing the use of ionizing radiation based modalities (X-ray/CT), which would lead to safer real-time imaging. This trend has the potential to impact a wide range of applications in orthopaedics. For example, tracked US could improve navigation of pedicle screw placement [1]. Intraoperative US could also supplement fluoroscopy-based procedures, such as pelvic fracture fixation [2,3]. In pediatric orthopaedics, Cheung et al. [4] demonstrated the potential benefits of US imaging in routine checkups of scoliosis patients. Furthermore, in spine imaging, US bone surface extraction was shown to be promising for needle-insertion applications [5].

Bone surface extraction based on the detection of symmetric response features was recently shown to be a powerful approach [6, 7]. However, local symmetry features remain prone to false detection of soft-tissue interfaces that often exhibit features similar to those of bone. Furthermore, though quite effective on relatively flat (i.e.

sparsely-oriented) structures, raw phase symmetry responses require tedious non-intuitive parameter tuning procedures to correctly identify complex bone shapes. Attempts to automate the parameter selection process have been made [7] but persistent false positives remain, especially at soft tissue interfaces. Apart from approaches based on local symmetry features, other bone-surface segmentation methods exist that exploit the bone shadowing effect and local image intensity. Foroughi et al. [8] used dynamic programming on intensity and local gradient information to segment bone contours in 2D images. The approach has shown adequate clinical accuracy in 2D US images, but it requires region-of-interest selection to remove soft-tissue interfaces near the skin surface and the method was only applied to 2D US images. Another bone contour detection scheme relied on depth weighted adaptive thresholding and subsequent morphological opening/closing operators to enhance segmented bone surfaces in 2D images [9]. A recent study used eigen-analysis information from a multi-scale 3D Hessian matrix to enhance sheet-like surfaces for the purpose of generating 3D segmentations of large bones [10]. However, results from these techniques remain heavily dependent on quality of the US image, as well as on the depth and complexity of the imaged bone due to the effects of shadowing and attenuation of local intensities.

Despite their aforementioned limitations, local image phase features were shown to be effective for bone segmentation in certain subsets of US images. We therefore hypothesized that identifying and integrating *additional* features of bone surfaces would increase robustness and accuracy of the segmentation. The first key feature we use is local phase symmetry (PS). As widely studied, bone surfaces in US typically exhibit ridge-like responses that are well captured by local image PS features [6]. To calculate those, we use a 3D log-Gabor filter as our quadrature filter since it can be constructed with arbitrary bandwidth. The second key feature of bone material that we use is its significantly higher US attenuation effect compared to other tissues, which results in the characteristic shadowing below the bone surface in the US image. To quantify this shadowing and attenuation feature, we employ Karamalis et al.'s [11] shadow detection algorithm, which extracts a transmission model for an US image. Finally, we combine the aforementioned features into a hybrid feature that we call confidence-in-phase-symmetry (CPS) and that is intended to augment the PS measure in regions where shadowing and attenuation is large. We limit our presentation to 3D due to space limitations and since a 2D version is a straight forward simplification that would instead use a 2D log-Gabor filter bank.

2 Methods

Given a 3D US volume, $I_{x,y,z}$, we first extract phase symmetry information, $PS_{x,y,z}$, using *uniformly oriented filters* (Section 2.1). To alleviate the challenging and time-consuming problem of precise tuning of filter parameters to reduce outliers, we supplement the PS measures using an attenuation metric, $A_{x,y,z}$, and a shadowing metric,

$S_{x,y,z}$ (section 2.2). We combine the three measures, $PS_{x,y,z}$, $A_{x,y,z}$ and $S_{x,y,z}$ (section 2.3) to generate our hybrid feature, $CPS_{x,y,z}$.

2.1 Local Phase Symmetry Feature

Similar to [6], we calculate a 3D PS measure from even and odd symmetric log-Gabor filter responses, denoted e_{rm} and o_{rm}, respectively, compensated by a noise power threshold, T_r, over all scales r and all orientations, m, with ε being a small number to prevent division by zero:

$$PS = \frac{\sum_r \sum_m \lfloor |e_{rm}| - |o_{rm}| \rfloor - T_r}{\sum_r \sum_m \sqrt{e_{rm}^2 + o_{rm}^2} + \varepsilon}. \quad (1)$$

In the frequency domain, the 3D log-Gabor filter bank has the transfer function:

$$3DG = exp[\frac{(log(\omega/\omega_{0i}))^2}{2(log(k/\omega_{0i}))}] * exp(-\frac{\alpha(\varphi_j,\theta_j)^2}{2\sigma_\alpha^2}), \quad (2)$$

where subscripts i and j represent a scale and an orientation, respectively, of the filter bank. k is the standard deviation of the Gabor filter in the radial direction and ω_{0i} is the central frequency. $\alpha(\varphi_i, \theta_i)$ controls the 3D orientation of the filter where φ_i and θ_i are the azimuth and elevation angles, respectively, and σ_α determines the angular bandwidth. The log-Gabor function is scaled with constant ratio filters by keeping the term k/ω_{0i} constant and using multiples of a minimum wavelength, λ_{min}.

2.2 Attenuation and Shadowing Feature

Similar to Karamalis et al. [11] we calculate a confidence map to quantify both the attenuation and shadowing properties in US images. We run a random walk [12] to calculate virtual signal strengths at every pixel in each ultrasound slice, given a signal being transmitted from virtual transducer locations at the top of the image slice. Essentially, the virtual signal strength of a pixel is the probability of a random walk (starting from the pixel itself), to reach the virtual transducers, and is computed from the graph Laplacian matrix. For different combinations of two nodes, v_i and v_j, the graph Laplacian matrix is defined as:

$$L_{ij} = \begin{cases} d_i & if\ i = j \\ -w_{ij} & if\ v_i\ adjacent\ to\ v_j \\ 0 & otherwise \end{cases}, \quad (3)$$

where w_{ij} represent the edge weights and $d_i = \sum_j w_{ij}$ [12]. This Laplacian matrix, L, is reformulated and decomposed into blocks of marked nodes, M, and blocks of unmarked nodes, with B being an incident matrix:

$$L = \begin{bmatrix} L_M & B \\ B^T & L_U \end{bmatrix}. \quad (4)$$

The solution for the desired unknown probabilities of unmarked nodes X_U can be found using $L_U X_U = -B^T X_M$, where X_M represents the known unit probabilities at the seed-points [11]. The edge-weights, w_{ij}, are then assigned in the horizontal, vertical and diagonal direction: $w_{ij}^H = \exp(-\beta(|c_i - c_j| + \gamma))$, $w_{ij}^V = \exp(-\beta(|c_i - c_j|))$, $w_{ij}^D = \exp(-\beta(|c_i - c_j|))$. The term, $c_i = g_i \exp(-\alpha l_i)$, is the depth-based intensity gradient controlled by parameter α, and γ represents the penalty of a horizontal and diagonal walk compared to a vertical walk. β controls robustness of the overall result of random walk. However, β barely affects the resulting confidence maps between the range $\beta = 90$ to $\beta = 120$ [11].

In a 2D ultrasound image $I_{x,y}$, the confidence map, $m_{x,y}$, resulting from the above-mentioned probability map, ranges between 0 to 1. The values can be interpreted as relative signal strengths at different image locations. We calculate a local attenuation measure, $A_{x,y}$, which has a value between 0 and 1:

$$A_{x,y} = \frac{\sum_w (m_{x,y} - m_{min})}{\max(\sum_w (m_{x,y} - m_{min}))}, \tag{5}$$

where w refers to 2D windows at multiple scales around $m_{x,y}$ of dimensions $\lambda_{min}/2$, $\lambda_{min}/4$ and $\lambda_{min}/6$, where λ_{min} is the lowest scale used in the PS calculation, and m_{min} is the corresponding minimum node values in the windows. $A_{x,y}$ tends to highlight bone surfaces due to the stronger reduction of signal strength, Δm, at the bone surface. Similarly, we measure a shadowing feature, $S_{x,y}$, which has a value between 0 and 1:

$$S_{x,y} = \frac{\sum_w m_{x,y}/(m_{min})}{\max[\sum_w m_{x,y}/(m_{min})]}, \tag{6}$$

which quantifies the shadowing effect at location (x, y). This feature is strong at points characterized by a relative deficiency in signal strength. Although $A_{x,y}$ and $S_{x,y}$ seem related, both are needed to better highlight bone surfaces. $A_{x,y}$ alone will tend to fail for deeper bone surfaces, whereas $S_{x,y}$ alone will tend to erroneously highlight US artifacts and noise below the actual bone surface.

Finally, we concatenate the responses measured in each 2D slice into 3D response images designated as $A_{x,y,z}$ and $S_{x,y,z}$. It is worth mentioning that a random walk in 3D may be more appropriate if the US transducer directly acquired 3D images. However, since our US transducer (Ultrasonix, 4DL14-5/38 Linear 4D) acquires a set of 2D images, separated spatially and temporarily, we opted to initially use a 2D random walk for our experiments.

2.3 Combined Feature for Bone Surface Localization

To combine the features, we define the bone membership probability:

$$P_{x,y,z} = \begin{cases} a_1 * A_{x,y,z} + a_2 * S_{x,y,z} + a_3 * PS_{x,y,z} & if\ PS > 0 \\ 0 & if\ PS = 0' \end{cases} \quad (7)$$

where a_1, a_2 and a_3 are weights. In our experimentation, we initially set each weight to 1/3. We defer the optimization of weights, a_1, a_2, a_3, for future work.

Along each column y in the metric, $P_{x,y,z}$, we identify the maximum value, and extract the corresponding voxel location, (x_m, y_m, z_m). These locations correspond to the highest bone surface membership confidence and thus can provide a more reliable bone segmentation mask. We evaluate the mean, μ, and the standard deviation, σ, of the confidence map values, $m(x_m, y_m, z_m)$, and formulate our final CPS feature as:

$$CPS_{x,y,z} = \begin{cases} P_{x,y,z} * PS_{x,y,z} & if\ |m_{x,y,z} - \mu| < \sigma \\ 0 & otherwise \end{cases} \quad (8)$$

Here, μ characterizes the statistical mean of the confidence map (or relative signal strength) values at the bone surface. We denote $\mu \pm \sigma$ to be the boundaries of the aforementioned mask. This formulation is based on the notion that the shadow just below the bone surface and the region just above the bone surface should ideally have similar patterns of confidence values, $m_{x,y,z}$.

3 Results and Discussion

To assess the performance of the CPS feature, we evaluated it on US image sets with corresponding CT data from an *ex-vivo* bovine femur phantom as well as from *in-vivo* pelvic data collected from 18 trauma patients (obtained as part of routine clinical care under appropriate institutional review board approval). We compare our proposed CPS method against a previously-reported version of PS [6]. The PS surface for both methods was based on empirical filter parameters set to values similar to those described in [6]: $scale = 1, k/\omega_{0i} = 0.25$, $\lambda_{min} = 25$, $\sigma_\alpha = 15°$, and $number\ of\ orientations = 6$. Also, similar to what was described in [11], we used $\alpha = 2$, $\beta = 90$, and $\gamma = 0.2$, for generating the confidence map. Throughout our study, these selected parameters were not changed.

The *ex-vivo* bovine femur (Fig. 1(a)) was placed in a polyvinyl chloride-filled cylindrical tube, with fiducials added to enable a direct comparison between the US and CT-derived surfaces. The bovine phantom represents a cylindrical (multi-directional) structure. Using the CT-derived surface (Fig. 1(b)) as the ground truth, we observed that the CPS-based surface (Fig. 1(e)) was able to remove considerably more soft-tissue outliers compared to PS alone (Fig. 1(d)).

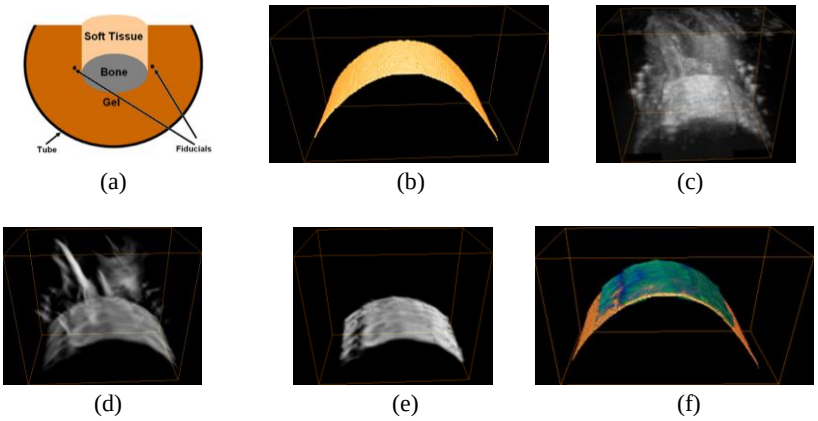

(a) (b) (c)

(d) (e) (f)

Fig. 1. Qualitative result on ex-vivo bovine femur data. (a) Bovine phantom setup, (b) CT volume showing segmented upper bone surface, (c) corresponding US volume, (d) PS, (e) proposed CPS, (f) overlay of segmented CT bone surface (orange) and extracted CPS based US bone surface (green).

To quantify the accuracy of segmentation, we registered the two surfaces (US-derived and CT-derived) using the fiducial locations. We then calculated a surface registration error (SRE) as the Euclidean root mean square distance between the segmented bone surfaces from the registered US and CT datasets [13]. The CPS algorithm produced a SRE of 0.236 mm, vs 0.538 mm for PS alone (Fig. 2(a)).

For the *in-vivo* pelvic data, where we do not have access to fiducial markers, we used *automatic* Gaussian mixture model (GMM)-based registration [13] to align the CT- and US-derived bone surfaces and computed the corresponding surface registration error (SRE) or surface fitting error (SFE), therefore avoiding any biases related to any landmark selection. The final bone surfaces that were used during the registration algorithm were determined from the maximum of feature responses along the direction of US probe. Results are summarized in Fig. 2(b).

Fig. 3 shows qualitative results of the CPS algorithm compared with two versions of the PS method, one using the empirical parameters described above and the other using optimized parameters determined as described in [7]. The optimization of parameters in [7, 13] relies on the assumption that bone surfaces will have the most significant ridge-like features in the ultrasound image, and performs a subsequent simplification of filter bank. Though successful in reducing soft-tissue outliers compared to empirical parameter-based PS, over-simplification may cause loss of true positives, as can be seen in the first example of Fig. 3. Also, note that some soft-tissue interfaces remain after optimized PS segmentation, since their response to the optimized filter bank is similar to that of bone surface. For both examples, the proposed CPS method appears to have improved bone surface segmentation, as illustrated in Fig.3.

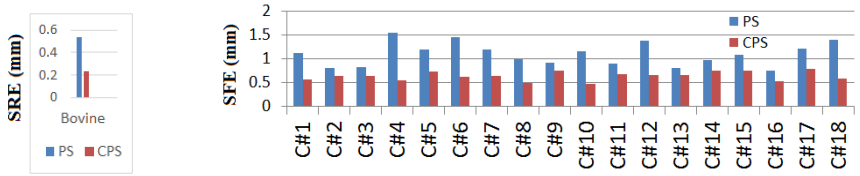

(a) (b)

Fig. 2. Quantitative results. (a) Bovine phantom. Note that our proposed CPS based segmentation resulted in a 0.302 mm reduction in error compared to PS. (b) In-vivo pelvic data across all subjects (C#1 to C#18). Note that our proposed CPS resulted in a reduction in error which is significant at ($p<0.0002$) based on Wilcoxon signed rank test compared to PS.

In terms of computational cost, for a 152×158×112 US volume, CPS required a small increase in run time with an average of 0.263 sec per US slice, compared to 0.216 sec for PS only. All tests were run on a Xeon(R) 3.40 GHz CPU computer with 8 GB RAM with MATLAB code.

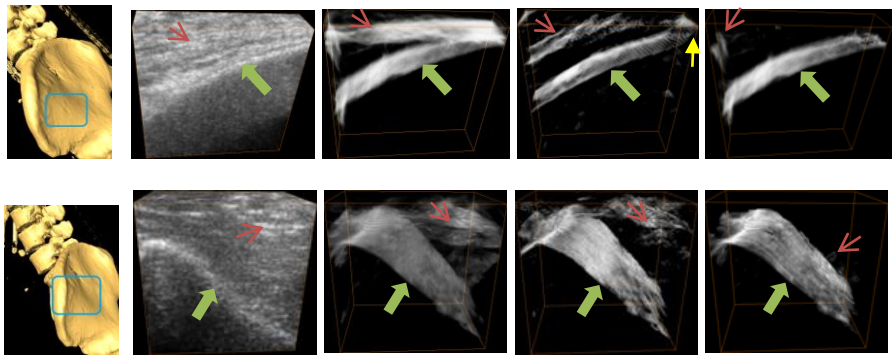

(a) (b) (c) (d) (e)

Fig. 3. Qualitative results: segmented bone surfaces around *in-vivo* pelvis, with two different US transducer locations and orientations. (a) Segmented CT with box representing approximate location of US transducer, (b) corresponding B-mode US volume, (c) PS based on empirical parameters, (d) PS based on optimized parameters [13], (e) proposed CPS feature based on augmented features with (b). Green arrows point to actual bone surfaces, red arrows point to soft-tissue interfaces, and the yellow arrow in the first example points to missing bone surface points. Our proposed CPS method appears to demonstrate qualitatively improved bone surface extraction and improved soft-tissue artifact reduction compared to both prior PS methods.

4 Conclusions

We proposed a novel US bone enhancement algorithm that builds on PS-based bone segmentation by augmenting PS with certainty cues generated by a random walk. We demonstrated that this new feature enables better bone surface segmentation with minimal need for parameter tuning and can be computed with relatively little additional time. This method is simple to implement and provides an intuitive combina-

tion of complementary bone surface features and robustness to soft-tissue outliers. We validated the algorithm on a bovine phantom and on *in-vivo* clinical pelvic data, and both qualitative and quantitative results suggest promising robustness across a number of bone surface geometries; in contrast, phase symmetry seems to be primarily effective on relatively flat surfaces. In future work, we plan to evaluate the sensitivity of this metric to the choice of weights for the different features and to apply the CPS metric to additional scenarios of clinical interest.

References

1. Ungi T., Moult E., Schwab J.H., Fichtinger G.: Tracked ultrasound snapshots in percutaneous pedicle screw placement navigation: a feasibility study. Clinical Orthopaedics and Related Research, vol. 471(12), pp. 4047-4055 (2013)
2. Amin D.V., Kanade T., Digioia A.M., Jaramaz B.: Ultrasound registration of the bone surface for surgical navigation. Journal of Computer Aided Surgery, vol. 8(1), pp. 1-16 (2003)
3. Tonetti J, Carrat L., Blendea S.: Clinical results of percutaneous pelvic surgery: Computer assisted surgery using ultrasound compared to standard Fluoroscopy. Journal of Computer Aided Surgery , vol. 6(4), pp. 204-211 (2001)
4. Cheung C.W., Law S.Y., Zheng Y.P.: Development of 3D ultrasound system for assessment of adolescent idiopathic scoliosis (AIS): and system validation. Conference Proceedings IEEE Engineering Medical Biology Society (2013)
5. Hacihaliloglu I., Rasoulian A., Rohling R. N., Abolmaesumi P.: Statistical shape model to 3D ultrasound registration for spine interventions using enhanced local phase features. MICCAI (2013)
6. Hacihaliloglu I., Abugharbieh R., Hodgson A.J., Rohling R.N.: Bone segmentation and fracture detection in ultrasound using 3D local phase features. MICCAI (2008)
7. Hacihaliloglu I., Guy P., Hodgson A., Abugharbieh R.: Volume-specific parameter optimization of 3D local phase features for improved extraction of bone surfaces in ultrasound images. International Journal of Medical Robotics and Computer Assisted Surgery (2013)
8. Foroughi P, Boctor E, Swatrz M.J., Taylor R.H., Fichtinger G.: Ultrasound bone segmentation using dynamic programming. IEEE Ultrasonics Symposium, pp. 2523–2526 (2007)
9. Kowal J., Amstutz C., Langlotz F., Talib H., Ballester M.G.: Automated bone contour detection in ultrasound B-mode images for minimally invasive registration in computer assisted surgery an in vitro evaluation. International Journal on Medical Robotics Computer Assisted Surgery, vol. (3), pp-341-348 (2007)
10. Fanti Z., Torres F.; Cosío F.A.: Preliminary results in large bone segmentation from 3D freehand ultrasound. International Seminar on Medical Information Processing and Analysis (2013)
11. Karamalis A., Wein W, Klein T., Navab N.: Ultrasound confidence maps using random walks. Medical Image Analysis, vol. 16, pp.:1101-1112 (2012)
12. Grady, L.: Random walks for image segmentation. IEEE Transactions on Pattern Analysis and Machine Intelligence, vol. 28, pp.:1768–1783 (2006)
13. Hacihaliloglu I., Brounstein A., Guy P., Hodgson A., Abugharbieh R.: 3D ultrasound-CT registration in orthopaedic trauma using GMM registration with optimized particle simulation-based data reduction". MICCAI, pp. 82-89 (2012)